remote sensing

MDPI

Article

Efficient On-Board Compression for Arbitrary-Shaped Cloud-Covered Remote Sensing Images via Adaptive Filling and Controllable Quantization

Keyan Wang [1,2,3], Jia Jia [1,2], Peicheng Zhou [1,2,*], Haoyi Ma [1,2], Liyun Yang [1,2], Kai Liu [4] and Yunsong Li [1,2]

[1] State Key Laboratory of Integrated Services Networks (ISN), Xidian University, Xi'an 710071, China; kywang@mail.xidian.edu.cn (K.W.); jiaj@stu.xidian.edu.cn (J.J.); mhy@stu.xidian.edu.cn (H.M.); 19011210511@stu.xidian.edu.cn (L.Y.); ysli@mail.xidian.edu.cn (Y.L.)
[2] School of Telecommunication Engineering, Xidian University, Xi'an 710071, China
[3] Hangzhou Institute of Technology, Xidian University, Hangzhou 311231, China
[4] School of Computer Science and Technology, Xidian University, Xi'an 710071, China; kailiu@mail.xidian.edu.cn
* Correspondence: zhoupeicheng@xidian.edu.cn; Tel.: +86-29-8820-3116

Abstract: Due to the fact that invalid cloud-covered regions in remote sensing images consume a considerable quantity of coding bit rates under the limited satellite-to-ground transmission rate, existing image compression methods suffer from low compression efficiency and poor reconstruction quality, especially in cloud-free regions which are generally regarded as regions of interest (ROIs). Therefore, we propose an efficient on-board compression method for remote sensing images with arbitrary-shaped clouds by leveraging the characteristics of cloudy images. Firstly, we introduce two novel spatial preprocessing strategies, namely, the optimized adaptive filling (OAF) strategy and the controllable quantization (CQ) strategy. Specifically, the OAF strategy fills each cloudy region using the contextual information at its inner and outer edge to completely remove the information of cloudy regions and minimize their coding consumption, which is suitable for images with only thick clouds. The CQ strategy implicitly identifies thin and thick clouds and rationally quantifies the data in cloudy regions to alleviate information loss in thin cloud-covered regions, which can achieve the balance between coding efficiency and reconstructed image quality and is more suitable for images containing thin clouds. Secondly, we develop an efficient coding method for a binary cloud mask to effectively save the bit rate of the side information. Our method provides the flexibility for users to choose the desired preprocessing strategy as needed and can be embedded into existing compression framework such as JPEG2000. Experimental results on the GF-1 dataset show that our method effectively reduces the coding consumption of invalid cloud-covered regions and significantly improve the compression efficiency as well as the quality of decoded images.

Keywords: remote sensing image compression; invalid cloud-covered regions; region of interest; spatial preprocessing; optimized adaptive filling strategy; controllable quantization strategy

check for updates

Citation: Wang, K.; Jia, J.; Zhou, P.; Ma, H.; Yang, L.; Liu, K.; Li, Y. Efficient On-Board Compression for Arbitrary-Shaped Cloud-Covered Remote Sensing Images via Adaptive Filling and Controllable Quantization. *Remote Sens.* **2024**, *16*, 3431. https://doi.org/10.3390/rs16183431

Academic Editor: Melanie Vanderhoof

Received: 11 July 2024
Revised: 4 September 2024
Accepted: 13 September 2024
Published: 15 September 2024

Copyright: © 2024 by the authors. Licensee MDPI, Basel, Switzerland. This article is an open access article distributed under the terms and conditions of the Creative Commons Attribution (CC BY) license (https://creativecommons.org/licenses/by/4.0/).

1. Introduction

As the resolution of aerospace optical remote sensing (RS) cameras increases rapidly, the volume of RS images grows exponentially [1,2]. However, the satellite-to-ground data transmission rate is not yet capable of meeting real-time requirements [3]. In order to receive these massive high-resolution RS images within a limited time, it is essential to adopt efficient image compression technology. Under the premise of guaranteeing the quality of the reconstructed RS images, lossy compression is able to produce a large data reduction, which greatly reduces the quantity of data to be transmitted. Therefore, compared to lossless compression, lossy compression has been a more suitable choice for on-board RS image compression.

Clouds are arbitrary-shaped, inevitable in RS images, and are usually regarded as invalid regions or non-ROIs due to the limited information they provide for typical RS applications (e.g., target detection and identification) [4]. Traditional image compression methods such as JPEG2000 suffer from low compression efficiency and poor reconstructed quality when compressing cloud-covered RS images on-board [5], because data in the cloud-covered region consume a considerable quantity of coding bit rates. Therefore, if the bit-rate consumption in cloudy regions can be reasonably removed or reduced during the compression process, the quality of reconstructed images can be significantly improved.

In recent years, various compression algorithms have been proposed for RS images containing invalid regions, which can be roughly categorized into two types: wavelet-based ROI coding algorithms and spatial preprocessing-based compression algorithms. The former type of method prioritizes encoding the wavelet coefficients of ROIs or directly skips the coefficients of invalid regions without coding, such as MaxShift [6], Scaling-based [7], shape adaptive wavelet transform (SA-DWT) [8], and shape adaptive bitplane coding (SA-BPE) [9]. The latter type of method first performs spatial preprocessing with a simple filling strategy to change the original pixel values of the invalid regions to some specific values and then compresses the preprocessed image by conventional image compression methods. Representative methods include Pagecyte, ADR [9], and LEC [10].

In comparison between these two categories of algorithms, the wavelet-based ROI coding methods can reduce the coding consumption of invalid regions, but they have high complexity and are suitable for RS images containing regularly shaped ROIs instead of arbitrarily shaped cloud-covered regions [11]. In contrast, the spatial preprocessing-based compression methods are simple and effective. More importantly, they are insensitive to the shape of ROIs and have better compatibility with various commonly used image compression methods such as JPEG2000. Therefore, the spatial preprocessing-based compression methods are more suitable for on-board compression of cloud-covered RS images.

However, the current spatial preprocessing-based compression methods suffer from three obvious shortcomings. (1) The filling strategy used in the existing spatial preprocessing is only applicable to RS images that contain thick clouds instead of thin clouds. This is because thick cloud-covered regions contain almost no valid information, their consumed bit rates can be greatly reduced by using the filling strategy. On the contrary, regions covered by thin clouds, to a certain extent, convey some useful information that would be lost by utilizing the filling strategy. (2) The compression performance of the existing methods is limited due to the inefficiency of the filling strategy. For example, the LEC [10] method with state-of-the-art performance adopts the filling strategy that only considers contextual information at the outer edge of the cloud-covered regions. If the cloud detection algorithm fails to accurately detect the edge of the clouds, the filling value of cloud-covered regions obtained by LEC would be inappropriate, resulting in a higher bit-rate consumption at cloud boundaries. (3) Most of the existing methods do not consider how to encode the cloud mask efficiently. In practice, the cloud mask should be encoded as side information and transmitted to the terrestrial decoder along with the image code stream. However, for a given compression ratio or total bit rate, inefficient coding for cloud mask would reduce the bit rate allocated to the RS image and degrade the quality of the restored image.

To address the above-mentioned issues, we propose an efficient on-board compression method for arbitrary-shaped cloud-covered RS images. The proposed method leverages the characteristics of cloud-covered RS images to effectively reduce the coding consumption of invalid cloud-covered regions and significantly improve the compression efficiency of ROIs as well as the quality of decoded images. To be specific, we first propose an optional spatial preprocessing mechanism including two novel preprocessing strategies: the optimized adaptive filling (OAF) strategy and the controllable quantization (CQ) strategy. The OAF strategy fills each cloudy region by taking into account the contextual information at its inner and outer edge, which can completely remove the information of cloudy regions and minimize their coding consumption. By leveraging the characteristics of the distribution

of thick and thin clouds and information redundancy in cloudy regions, the CQ strategy implicitly identifies thin and thick clouds and rationally quantifies the data in cloudy regions. It can alleviate information loss caused by the thin cloud-covered regions being filled as a fixed value and achieve the balance between coding efficiency and reconstructed image quality. The optional preprocessing mechanism provides the flexibility for users to choose the desired preprocessing strategy as needed and can be embedded into existing compression framework. Secondly, we propose an efficient coding algorithm for the binary cloud mask by exploiting the spatial correlation of the mask and the characteristics of the ROI mask symbol sequences. The algorithm skillfully integrates block coding, run-length coding, and Huffman coding, which effectively reduces the bit rate of the cloud mask, and improves the coding efficiency and the subjective visual quality of the decoded images. Thirdly, we optimize the DC level shift module in the mainstream compression algorithms (such as JPEG2000) to make it more suitable for cloud-covered remote sensing images.

Our contributions are mainly summarized as follows.

(1) By leveraging the characteristics of cloud-covered remote sensing images, we propose an efficient on-board compression method based on an optional spatial preprocessing mechanism including the optimized adaptive filling (OAF) strategy and the controllable quantization (CQ) strategy for RS images containing arbitrary-shaped clouds. Our method can effectively reduce the coding consumption of invalid cloud-covered regions and significantly improve the compression efficiency of ROIs as well as the quality of reconstructed images.

(2) By analyzing the local edge characteristics of cloudy regions, we propose the OAF strategy, which uses the mean of the inner and outer edges to fill the cloudy regions. It minimizes the gray-scale value difference between cloudy regions and cloud-free regions and prevents the loss of cloud edge information. After filling, the mean filtering is then performed on the edges to make it smooth, which fully reduces the high-frequency wavelet coefficients at the edges and further improves compression performance. The OAF strategy can achieve minimum bit rates and is suitable for images with only thick clouds.

(3) We skillfully design a flexible CQ strategy which can implicitly identify thin clouds and thick clouds. By setting the quantization factor and sampling factor, the data in cloudy regions can be reasonably quantized in the amplitude domain and the spatial domain, respectively. The CQ strategy not only eliminates invalid information and reduces coding consumption but also retains the partial information of ground objects in thin cloud-covered regions, which can balance compression efficiency and image restoration quality and is more suitable for images containing thin clouds. In particular, when extreme quantization is used, i.e., the quantization factor of the CQ strategy is maximum, the CQ strategy degenerates into the OAF strategy.

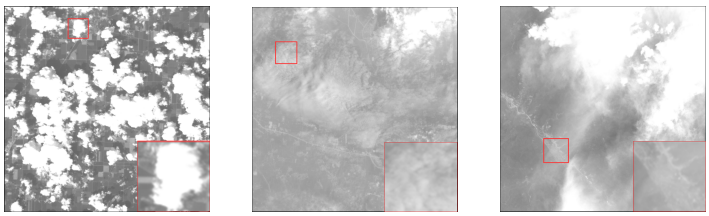
(4) Taking advantage of the spatial correlation of the binary mask and the characteristics of the ROI mask symbol sequence, we propose an efficient binary cloud mask coding algorithm. The algorithm skillfully combines block coding, run-length coding, and Huffman coding. Firstly, a block scan is used for the entire image. Secondly, run-length coding is used for the regional block symbols with a high probability of occurrence and strong continuity, which not only improves the coding efficiency of region unit symbols but also makes the whole symbol sequence coding more efficient and minimizes its proportion in the entire bitstream.

The rest of this paper is structured as follows. In Section 2, we analyze the characteristics of cloud-covered remote sensing images. In Section 3, we introduce in detail the proposed compression method for arbitrary-shaped cloud-covered RS images. In Section 4, we conduct comprehensive experiments to evaluate the compression performance of our method. Finally, we draw conclusions in Section 5.

2. Characteristics of Cloud-Covered Remote Sensing Images

Although clouds have arbitrary and different shapes, they can usually be categorized into thick and thin clouds based on the appearance characteristics of clouds in remotely sensed images [12]. The two categories of clouds are defined in this paper as follows:

(1) **Thick clouds**: one type of thick cloud completely occludes ground scenes, as shown in the red box of Figure 1a; the other type can transmit some light but seriously affects the interpretation of ground scenes, as shown in the red box of Figure 1b.
(2) **Thin clouds**: thin clouds can transmit light, which increases the brightness of images and causes blurring but does not affect the interpretation of ground scenes, as shown in the red box of Figure 1c.



(**a**) (**b**) (**c**)

Figure 1. The categories of clouds in the remote sensing image. (**a**,**b**) are thick clouds, (**c**) is thin cloud. The close-up views of the regions marked by red boxes are shown at the bottom right corner.

Cloud-covered remote sensing images, in comparison with cloud-free remote sensing images, have different characteristics, which are mainly manifested in the following aspects.

(1) **Intensity distribution**: Generally speaking, the statistical properties of the intensity (or gray-scale values) of pixels in cloud-free RS images conform to a normal distribution [13], as shown in Figure 2. However, in cloud-covered RS images, thick cloud-covered regions exhibit the highest brightness, while the intensity values of ground objects are relatively lower. Thin cloud-covered regions have intensity levels that are close to or slightly higher than ground objects. As shown in Figure 3, the intensity histogram of pixels in cloud-covered RS images shows a characteristic dual-peak distribution. Pixels in thick cloud-covered regions tend to cluster at higher gray-scale values, forming one peak, and pixels in cloud-free regions that contain ground objects form the other peak at lower gray-scale values. For example, in an 8-bit image, the gray-scale values of typical RS images are mostly distributed within the interval [0,255], whereas the gray-scale values of ground objects in cloud-covered RS images are primarily distributed within the interval [0,200], as shown in Figure 3. Furthermore, some cloudy regions may be missed, which leads to their intensity histogram no longer conforming to the normal distribution but to a long-tailed distribution, as shown in Figure 3d,i,n. In order to avoid the influence of these characteristics, we improve the level-shifting module of existing compression algorithms, which is described in detail in Section 3.4.
(2) **Texture**: In cloud-covered RS images, the texture of the cloudy region is relatively simple. A large number of pixels in cloudy regions have the same gray-scale value, which makes the intensity distribution relatively concentrated, as shown in Figure 3e,j,o. Therefore, there is a large amount of redundancy in cloudy regions. In the compression process of our method, cloudy regions can be downsampled to reduce the encoding rate. Meanwhile, the texture information of cloudy regions is not completely lost. This is described in Section 3.2.
(3) **Reflectivity**: The same object has different electromagnetic wave reflection characteristics for different wavelengths [14]. The reflectivity of thick clouds is very high, and electromagnetic wave radiation cannot penetrate them [15]. Sensors cannot detect ground objects occluded by thick clouds. Therefore, thick cloudy regions in RS images do not contain information on ground objects. It is reasonable to use a fixed value to

replace the gray values of pixels in thick cloudy regions, which can effectively reduce the encoding rate of the data in cloudy regions. This is the core idea of our proposed OAF strategy, which is introduced in Section 3.1. However, thin clouds have low reflectivity and are easily penetrated by solar radiation. Sensors can penetrate thin clouds to obtain some effective information on ground objects. Therefore, considering partial ground objects existing in thin cloudy regions, we propose a CQ strategy to retain the information on ground objects in thin cloudy regions. It is introduced in Section 3.2.

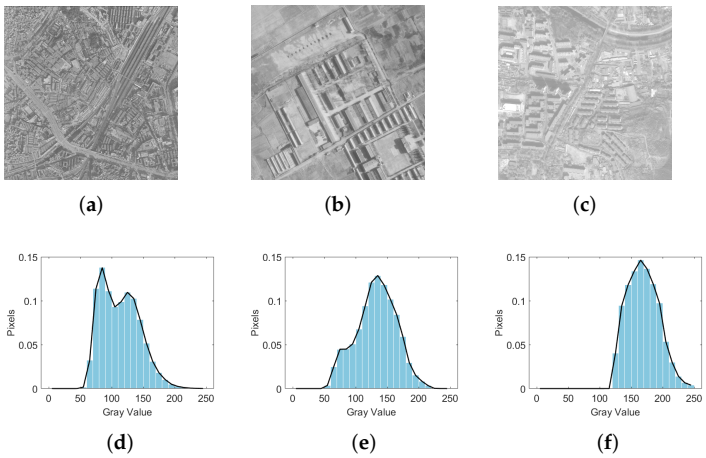


Figure 2. Intensity histograms of cloud-free remote sensing images. (**a**–**c**) are the original images. (**d**–**f**) are the corresponding gray value histograms of (**a**–**c**), respectively.

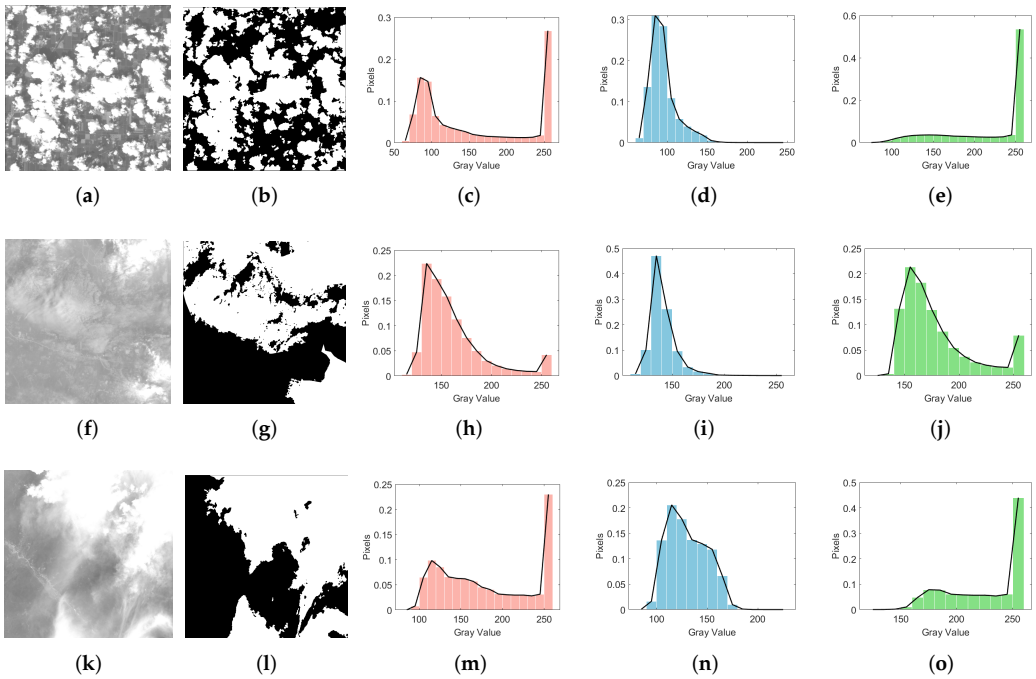


Figure 3. Intensity histograms of cloud-covered remote sensing images. (**a**,**f**,**k**) are the original images. (**b**,**g**,**l**) are cloud masks of (**a**), (**f**), (**k**), respectively. (**c**,**h**,**m**) are histograms of (**a**), (**f**), (**k**), respectively. (**d**,**i**,**n**) are histograms of ground object of (**a**), (**f**), (**k**), respectively. (**e**,**j**,**o**) are histograms of cloudy regions of (**a**), (**f**), (**k**), respectively.

(4) **Frequency**: In cloud-covered RS images, the hue of cloudy regions is uniform, and the texture structure is simpler than that of other ground objects, which makes cloudy

regions mainly contain low-frequency information in the frequency domain. In comparison with cloudy regions, rich and various ground objects mainly contain high-frequency information in the frequency domain [16]. Considering the gray-scale values of pixels in cloudy regions are significantly higher than those of most ground objects (e.g., water surface, vegetation, bare land, etc.), the adjacent boundaries between cloudy regions and ground objects contain more high-frequency components, which affect the image compression performance. To mitigate this effect, in the proposed OAF strategy, we fill each cloudy region with a fixed value that is closest to ground objects and then perform boundary filtering. In the CQ strategy, we smooth the adjacent boundaries by subtracting each connected cloudy region from the difference between the average values of its inner and outer edge context data. The specific processing details are described in Sections 3.1 and 3.2, respectively.

3. Methods

By analyzing and utilizing the characteristics of cloud-covered RS images, we developed an efficient compression method for arbitrary-shaped cloud-covered RS images. The main idea of our method is to reduce the coding rate of invalid cloudy regions and increase that of ROIs, thus improving the quality of decoded images. The overall codec framework is shown in Figure 4, where the pink boxes are relevant modules proposed in this paper.

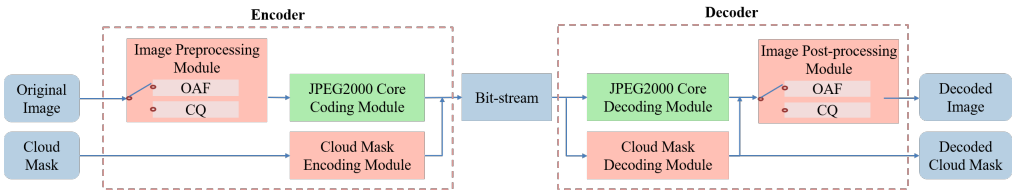


Figure 4. The overall codec framework.

The encoder mainly includes an image preprocessing module, a cloud mask encoding module, and a core coding module. The image preprocessing module includes two strategies, namely, the optimized adaptive filling strategy (OAF) and the controllable quantization strategy (CQ). These two strategies provide an optional preprocessing mechanism for users to manually choose the desired preprocessing strategy according to their needs. The image preprocessing module is generic and can be embedded into existing compression frameworks. The advantage of OAF is that the pixels of each cloudy region are filled with a fixed value, which can minimize the coding rate of invalid cloudy regions and increase the coding rate of ROI. Compared with the preprocessing modules of existing RS image compression methods, OAF achieves the best performance. The advantages of CQ are mainly manifested in two aspects. On the one hand, CQ has two parameter settings for cloudy region coding, i.e., a quantization factor and a sampling factor, which is more flexible than OAF in bit-rate adjustment. On the other hand, by setting the appropriate quantization factor and sampling factor, CQ can retain more information about ground objects in thin cloudy regions at low bit rates, which is lost in the preprocessing modules of existing RS image compression methods. The implementations of these two preprocessing strategies are described in Sections 3.1 and 3.2, respectively.

The cloud mask encoding module encodes irregular pixel-level cloud masks by using a blocking encoding technique, which is described in Section 3.3. Note that the cloud mask acquisition method was not the focus of our work because existing cloud detection methods are more mature and the accuracy of their cloud masks reaches more than 90% [17,18], so we directly used the existing cloud detection method such as [17] to acquire the cloud masks. The core coding module can be any state-of-the-art image compression algorithm. JPEG2000 is the more widely used on-board image compression algorithm. It is easy to implement and can achieve accurate bit-rate control while maintaining high compression performance [19]. Therefore, we chose JPEG2000 as the core coding module. Considering

the special gray-value distribution of cloud-covered RS image, we improved the DC level shift module of JPEG2000. The implementation details are described in Section 3.4. The bitstream is obtained by the encoder with the three modules.

The decoder mainly includes a core decoding module, a cloud mask decoding module, and an image post-processing module. The core decoding module and the cloud mask decoding module correspond to the core compression module and the cloud mask encoding module of the encoder. The decoded cloud mask provides the position information of cloudy regions and ROIs for the image post-processing. The image post-processing module is to increase the overall contrast of decoded images, which can improve the subjective visual quality of decoded images. It is introduced in Section 3.5.

3.1. Optimized Adaptive Filling Strategy

In cloud-covered RS image compression, an ROI can only allocate relatively low bit rates due to cloudy regions occupying a large number of bits, which results in poor-quality decoded images. To allocate bit rates reasonably, we removed the raw data in cloudy regions and fill them with a fixed value, which could keep cloudy regions at low compression bit rates. The filling value setting needed to consider the following aspects comprehensively.

(1) Recently, most image compression algorithms have mainly focused on eliminating the correlation among adjacent pixels in the time domain (such as predictive coding) or transform domain (such as DWT [20] or DCT) [21,22]. For prediction-based coding algorithms, smaller prediction errors bring lower coding costs. For transform-based coding algorithms, to obtain lower coding costs, the transformed high-frequency coefficients should be made as small as possible. To this end, the filling value of a cloudy region should be set as close as possible to the gray value of pixels in adjacent areas.

(2) Generally, cloud masks are obtained by cloud detection algorithms. Although existing cloud detection algorithms usually have an accuracy of more than 90%, there is a possibility of missed detection for thin cloud regions and some thick cloud regions [23]. Therefore, the filling value is required to be close to the gray values of pixels in missing cloudy regions and ROIs at the same time so that the balance between them is reached and coding costs can be reduced.

(3) In cloud-covered RS images, cloudy regions may appear randomly at any location, and the ground objects occluded by clouds are also diverse. A single filling value cannot represent the adjacent information of different cloudy regions. Therefore, different cloudy regions should set different filling values to represent their adjacent information.

Based on the above analyses, we propose an OAF strategy to set filling values for cloudy regions. As shown in Figure 5, OAF first employs the connected-component labeling algorithm [24–26] to mark all connected regions in the cloud mask, denoted as R^n, where n is the label of each cloudy region. Then, the inner and outer edges are obtained by subtracting the cloud mask after dilating from that after eroding [27], denoted as $\Phi_{doubleedge}$. Finally, the connected cloudy region is filled by the average y^n of the inner and outer edge data y,

$$\hat{y}^n = \frac{1}{N} \sum_{y^n \in \Phi^n_{doubleedge}} y^n, n = 0, 1, 2, \cdots, M, \tag{1}$$

where N is the number of pixels in the context of the inner and outer edges. M is the number of connected cloudy regions in the cloud mask.

Moreover, to further reduce the coding cost of the boundary between cloudy regions and ROIs, we smooth the boundary by mean filtering, which can decrease the high-frequency coefficients. As shown in Figure 6, where the white area is the cloudy region, the blue area is the ROI, and the red area is the pixel to be processed. We scan the cloudy region-filled image line-by-line. For each pixel, we determine whether the pixels of

ROI exist in its 4-neighborhood U_4. If it exists, the gray value y of the corresponding pixel in cloudy region is updated to $\hat{y} = \left\lfloor \frac{y+p}{2} \right\rfloor, p \in U_4, y \in \Phi_{cloud}$; otherwise, it is not updated. The scanning priority of the 4-neighborhood is up, left, right, and down.

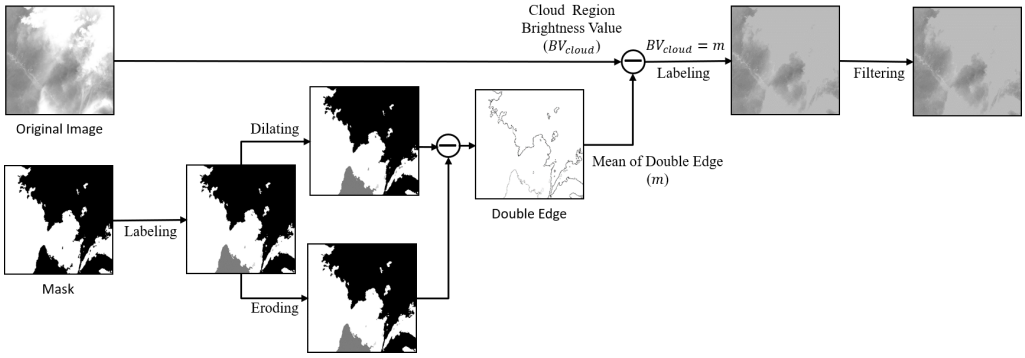


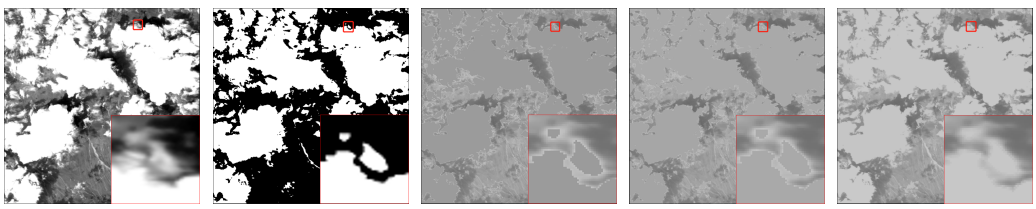
Figure 5. The processing flow of the optimized adaptive filling strategy.



(**a**) Original gray values of pixels (**b**) Processed gray values of pixels

Figure 6. Schematic diagram of boundary filtering on the filled cloudy region.

Figure 7 shows the comparison of cloudy region filling between the OAF strategy and the preprocessing modules of other existing image compression methods. It can be seen that the boundaries processed by OAF are smoother. Therefore, the high-frequency coefficients at the boundaries are smaller, which can make the coding cost of boundaries lower.

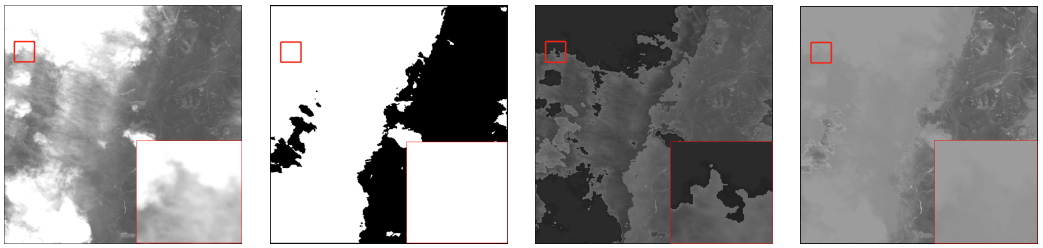


(**a**) (**b**) (**c**) (**d**) (**e**)

Figure 7. Comparison of cloudy region filling by using the preprocessing modules of different image compression methods. (**a**) is original image. (**b**) is cloud mask of (**a**), where white regions (gray value of 255) denote clouds and black regions (gray value of 0) denote ground objects. (**c**–**e**) are results of filling the cloudy region using ADR, LEC, and OAF (our method), respectively. The close-up views of the regions marked by red boxes are shown at the bottom right corner, which clearly shows the smoothness of the boundary after filling cloudy regions with different strategies.

3.2. Controllable Quantization Strategy

Thin cloud-covered regions contain both clouds and ground objects. In some cases, it is probable that the information on these ground objects plays a key role in task processing. Thus, in cloud-covered RS image compression, it is necessary to retain the information of ground objects in thin, cloudy regions. However, existing RS image compression algorithms discard the information of thin cloud-covered ground objects. To this end, we utilized different strategies to encode thin cloudy regions and thick cloudy regions. A straightforward way to distinguish thin clouds from thick clouds is to set a threshold. However, it is difficult to objectively set an accurate threshold for distinguishing thin clouds from thick clouds, and it is often required to set different thresholds for different images, which leads to a complex implementation and low accuracy. In addition, employing different strategies for thin clouds and thick clouds can easily generate high-frequency coefficients at the boundary between thin and thick clouds, which can increase coding costs and affect compression performance, as shown in Figure 8c. In this paper, we propose a controllable quantization (CQ) strategy, which not only ensures better compression performance but also retains the information of thin cloud-covered ground objects. The processing flow is shown in Figure 9.



(**a**) (**b**) (**c**) (**d**)

Figure 8. Results of different quantization methods. (**a**) is original image. (**b**) is cloud mask of (**a**). (**c**) is the result of quantization.(**d**) is the result of CQ. The close-up views of the regions marked by red boxes are shown at the bottom right corner.

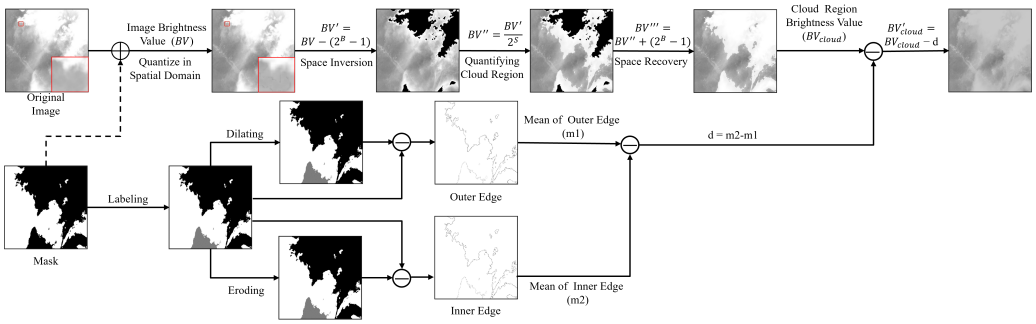


Figure 9. The processing flow of the controllable quantization strategy. The close-up views of the regions marked by red boxes are shown at the bottom right corner.

To be specific, the CQ first sets a sampling factor D and a quantization factor S to quantize the data in cloudy regions in the spatial domain and the amplitude domain, respectively, which reduces the coding rate of the data in cloudy regions. Secondly, the CQ employs the connected-component labeling algorithm [24–26] to mark all connected regions in the cloud mask. The outer edges are obtained by subtracting the dilated cloud mask from the labeled cloud mask, denoted as $\Phi_{outeredge}$. The inner edges are obtained by subtracting the eroded cloud mask from the labeled cloud mask, denoted as $\Phi_{inneredge}$. Finally, the gray values of pixels in cloudy regions are subtracted from the difference between the average values of inner and outer edges, which can increase the smoothness of the boundaries between cloudy regions and ROIs. Therefore, it can decrease high-frequency coefficients at the boundary and further improve image compression performance.

(1) Quantization of the data in cloudy regions in the spatial domain

In cloud-covered remote sensing images, there is a large amount of data redundancy due to the texture of cloudy regions being relatively simple. To remove the redundant data and reduce the coding rate of pixels in cloudy regions, as shown in Figure 10, we downsample the original image by setting a sampling factor D and then resize the downsampled image to the size of the original image by utilizing bilinear interpolation. Moreover, we fill ROIs with their average values before implementing quantization, which can largely reduce the coding cost of the bilinear interpolation.

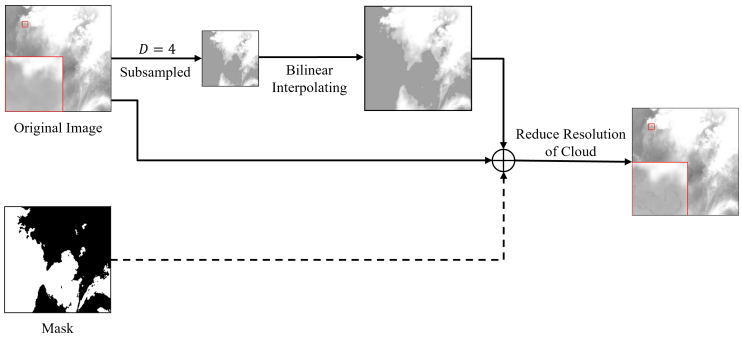


Figure 10. The quantization of the data in cloudy regions in the spatial domain. The close-up views of the regions marked by red boxes in the original image are shown at the bottom left corner.

(2) Quantization of the data in cloudy regions in the amplitude domain

In cloud-covered remote sensing images, thick cloudy regions have the highest pixel gray values in general and do not contain any ground objects, while the gray value of pixels in thin cloudy regions is lower, and the thin cloudy regions contain part of the ground objects. If the quantization factor S is directly used for quantization, pixels with gray values less than 2^s are quantized to 0. As a result, the information on the ground objects at this position is lost in the decoded image. For this reason, before performing quantization in the amplitude domain, we first subtract $2^B - 1$ (B is the image accuracy) of each pixel in the image Φ to invert gray values so that the gray values of pixels in thin cloudy regions is larger than that in thick cloudy regions. Then, we quantize cloudy regions Φ_{cloud}. After that, $2^B - 1$ is added to restore the spatial distribution of the original image. There is no loss of information in the above operations. The processing is formulated as Equations (2)–(4). The results of different quantization methods are shown in Figure 8. Figure 8a is the result of quantization after dividing thin clouds and thick clouds by using a threshold segmentation method, which sets the threshold as 200, the quantization of thin cloud as 1 bit, and the quantization of thick clouds as 3 bits. The results show that there is a clear boundary between thin and thick clouds after quantization, generating a large number of high-frequency coefficients at the boundary, which deteriorates the performance of image compression. Furthermore, the boundary cannot be smoother even by filtering. Figure 8d is the result of the CQ strategy, which sets the quantization factor as 4. As can be seen, there are no obvious boundaries between the thin clouds and the thick clouds.

$$y_1 = y - \left(2^B - 1\right), y \in \Phi, \tag{2}$$

$$y_2 = \frac{y_1}{2^s}, y_1 \in \Phi_{cloud}, \tag{3}$$

$$\hat{y} = y_2 + \left(2^B - 1\right), y_2 \in \Phi. \tag{4}$$

(3) Smoothness of boundaries

After quantization, there is a large difference between the gray values of the pixels in cloudy regions and those in ROIs. To smooth the boundaries, we subtract the gray values of the pixels in cloudy regions from the difference of the average value of its inner and outer edges. The result after smoothing denotes $\hat{y}^n$.

$$A^n = \frac{1}{N_1} \sum_{y^n \in \Phi^n_{outeredge}} y^n - \frac{1}{N_2} \sum_{y^n \in \Phi^n_{inneredge}} y^n, n = 0, 1, 2, ..., M, \quad (5)$$

$$\hat{y}^n = y^n -^A n, y^n \in \Phi^n_{cloud}, \quad (6)$$

where A^n denotes the difference of the average value of its inner and outer edges. N_1,N_2 are the number of pixels in the outer edge and inner edge. M is the number of connected cloudy regions in the cloud mask.

In summary, the CQ strategy quantizes cloudy regions in the amplitude and spatial domains, respectively. It can decrease the coding rate of cloudy regions and increase the coding rate of ROIs. Setting an appropriate quantization factor can improve compression performance and retain the information of thin cloudy regions.

3.3. Binary Cloud Mask Coding

Traditional mask coding methods [28,29] first flatten a 2D mask into a 1D vector and then perform entropy coding or run-length coding on the 1D vector. However, these methods do not consider the spatial correlation of the 2D mask. To address this issue, we employ block coding [30] to mask coding and optimize it from source and coding aspects. The proposed binary cloud mask coding method combines block coding, run-length coding, and Huffman coding. The processing flow is shown in Figure 11, whereas the symbol packing process is shown in Figure 12.

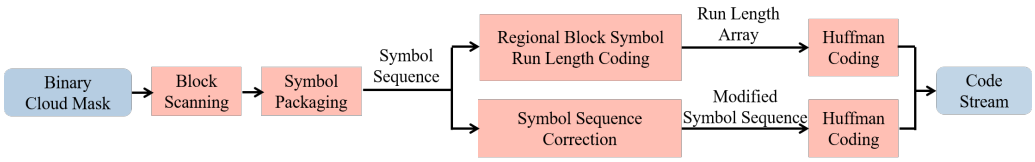


Figure 11. The processing flow of binary cloud mask encoding.

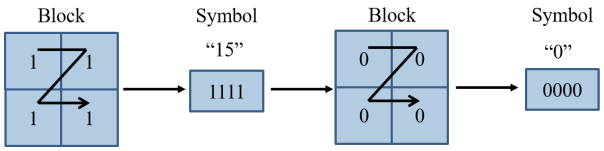


Figure 12. The processing flow of symbol packaging.

According to the above characteristics, we adopt a partial run-length coding method. Specifically, we only use run-length coding for the regional block symbols and calculate the run-length array. Then, the corresponding continuous regional block symbol is replaced with a symbol, which modifies the symbol sequence. Finally, Huffman coding is performed on the run-length array and the modified symbol sequence, respectively. Moreover, to avoid the code table of the run-length sequence occupying more bytes on run-length coding, we set a reasonable threshold of run length by comparison experiments. If the run length exceeds the threshold, a segment count is performed so that the number of bytes occupied by the entire bitstream is further decreased.

This method takes advantage of the characteristics of the binary mask symbol sequence and uses more efficient run-length coding for the regional block symbols with a high probability of occurrence and strong continuity. Moreover, since the original symbol

sequence is modified, the bitstream of some edge block symbols is saved, which can make the coding of the entire symbol sequence more efficient.

3.4. DC-Level Shift Optimization

The purpose of the DC-level shift is to remove the DC component in an image so that the probability of the positive and negative values of the coefficients after wavelet transformation is almost equal. This operation can further improve the efficiency of adaptive coding [31]. In fact, JPEG2000, CCSDS-IDC [32], and other state-of-the-art image compression algorithms perform DC-level shifting. Specifically, unsigned sample values in each component are level-shifted by subtracting a fixed value of 2^{B-1} from each sample to make its value symmetric around zero. Signed sample values are not level-shifted [6]. However, in cloud-covered RS images, the pixels of ROIs are mainly distributed in the low gray-value range, so the gray-value histogram of pixels in ROIs has long-tail characteristics. To solve this problem, we modified the original offset value 2^{B-1} to the median of the ROI. It can sufficiently ensure that the gray values of pixels in ROIs are symmetric around zero after DC-level shifting so that the dynamic range of the coefficients after wavelet transformation are not too large. The optimized DC-level shift method is conducive to encoding, which can improve the compression performance of ROIs and the quality of decoded images.

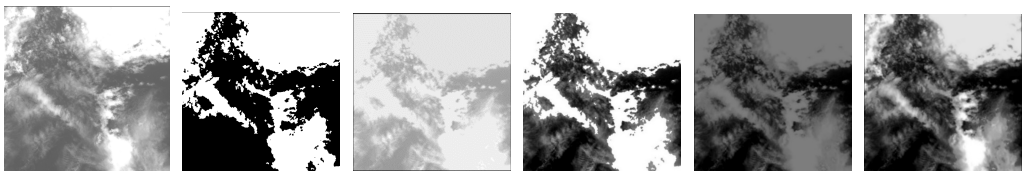
3.5. Image Post-Processing

Due to the influence of image preprocessing on the filling and quantization of cloudy regions, the gray values of pixels in the cloudy regions of decoded images are low. It is impossible to accurately distinguish cloudy regions from ROIs. To ensure a good subjective visual effect, image post-processing operations are added to enhance the contrast of decoded images.

In fact, the OAF eliminates the original data in cloudy regions, and the CQ narrows the range of data in cloudy regions. To enhance the contrast of decoded images, we fill cloudy regions by using the median of the original data in cloudy regions and then employ Gamma transformation [33] to expand the gray values of the pixels in cloudy regions. The principle of Gamma transformation is as follows.

$$S = cr^{\gamma}, \tag{7}$$

where c is a scaling factor and is usually set to 1, which can increase the gray level of the entire image. γ is the gray value. If $\gamma < 1$, the lower gray values are expanded. If $\gamma > 1$, the higher gray values are expanded. To expand the gray values of the pixels in cloudy regions, γ was set to 1.2. As shown in Figure 13, the contrast of the decoded images is significantly improved after post-processing so that cloudy regions and ROIs can be easily distinguished.



(**a**) (**b**) (**c**) (**d**) (**e**) (**f**)

Figure 13. The contrast of the decoded images before and after image post-processing. (**a**) is original image, (**b**) is cloud mask of (**a**). (**c**) OAF without post-processing, (**d**) OAF with post-processing, (**e**) CQ without post-processing, (**f**) CQ with post-processing.

4. Experiments

4.1. Dataset and Evaluation Metric

We used GF-1 images for the evaluation. The "Gaofen-1" satellite is a civilian HDEOS program launched by the China Aerospace Science and Technology Corporation (CASC) in April 2013 to achieve a high-resolution and wide-range optical remote sensing mission. We selected 108 full-scene panchromatic remote sensing images from GF-1 images as the evaluation dataset [34]. The dataset contained a total of 360 images with different types of land cover, including forest, ice/snow, water, urban area, farmland, etc. The average percentage of clouds on the dataset was about 50%. The image size was 1024 × 1024. The accuracy of images was 10 bits, and the accuracy of their cloud mask was 8 bits. Some examples of the evaluation dataset are shown in Figure 14a–e. All the experimental images below are displayed with automatic contrast processing through PhotoShop.

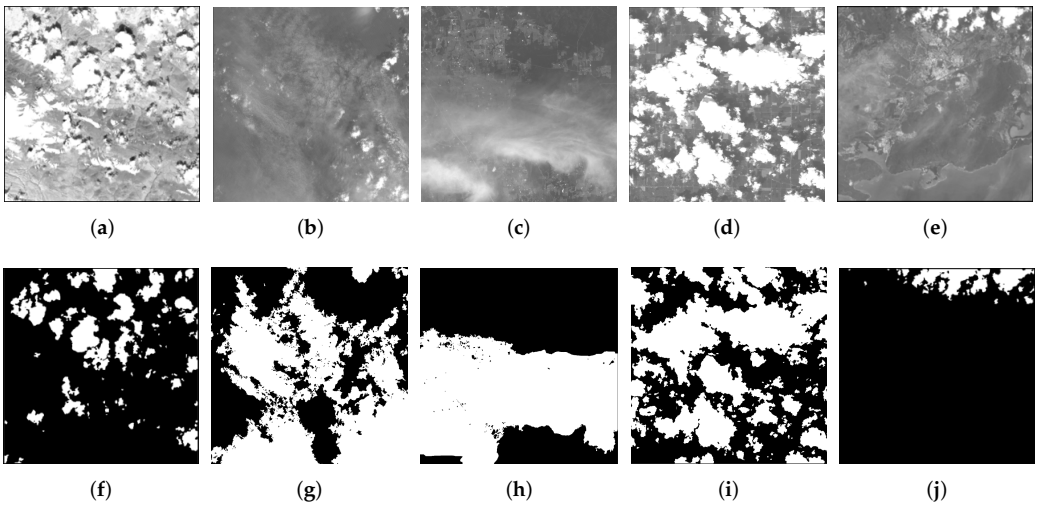


Figure 14. Examples of evaluation dataset. (**a**–**e**) are GF-1 remote sensing images including ice and snow, water, urban area, farmland, and forest, respectively, (**f**), (**g**), (**h**), (**i**), (**j**) are the corresponding cloud masks of (**a**), (**b**), (**c**), (**d**), (**e**) respectively.

To quantitatively evaluate the proposed method, we employed the peak signal-to-noise ratio of ROI ($PSNR_{ROI}$) as the evaluation metric, which is defined as

$$PSNR_{ROI} = 10log_{10}\frac{(2^B - 1)^2}{MSE_{ROI}}, \tag{8}$$

where B is the accuracy of the image, and MSE_{ROI} is the mean square error of ROI, which is defined as

$$MSE_{ROI} = \frac{\sum_{y \in \Phi_{ROI}} (y - \hat{y})^2}{N}, \tag{9}$$

where y is the gray value of the ROI in the original image, $\hat{y}$ is the gray value of the ROI in the decoded image, and N is the number of pixels in the ROI.

4.2. Optimal Length Threshold Setting of Cloud Mask Encoding Module

In the cloud mask encoding module, we set a reasonable threshold of the run length to decrease the entire bitstream. More detailed descriptions are provided in Section 3.3. To this end, we conducted experiments to test the consumption of each part of the binary cloud mask compression bitstream under different thresholds. The results are shown in Table 1. Finally, we chose the optimal threshold that had the smallest total consumption. Several binary cloud masks used in the test are shown in Figure 14f–j.

Table 1. The bitstream size of the cloud mask under different thresholds (Byte).

Threshold	Size of Each Part of the Bitstream (Byte)					
	Head	**Code Table1**	**Code Table2**	**Data1**	**Data2**	**Sum**
No threshold	15	77.5	2544.7	4286.7	4535.7	11459.5
256	14	77.5	1146.3	4349.6	4613.2	10200.5
192	14	77.5	928.3	4403.6	4652.3	10075.7
128	14	70.4	642.5	4182.9	4449.0	9358.8
96	14	77.5	485.0	4640.0	4756.6	9973.1
64	14	77.5	325.0	4884.3	4810.1	10110.9

In Table 1, "**Head** " denotes the basic information of the binary cloud mask image contained in the code stream. "**Code Table1**" and "**Code Table2**" denote the code table for Huffman coding of the run length array and the modified symbol sequence, respectively. "**Data1**" and "**Data2**" denote the run length array and the edge block symbol information, respectively.

By analyzing and comparing the bitstream size of the cloud mask with different thresholds in Table 1, it can be seen that as the threshold decreased, the size of the bitstream first decreased and then rose. When the threshold was set to 128, the total bitstream size was the smallest. As a result, 128 was the best threshold for the cloud mask coding to ensure better compression performance.

Table 2 shows that the method achieved higher compression efficiency, only slightly inferior to the CCITT-G4 and JBIG1 methods [35,36]. Although JBIG1 and CCITT-G4 provided better compression performance, they both had much higher coding complexity, which limited their on-board application.

Table 2. The bitstream size of the cloud mask compressed by different algorithms (KB).

	ZIP	**7Z**	**RAR**	**CCITT-G3**	**Our Method**	**CCITT-G4**	**JBIG1**
Size (KB)	15.1	14.9	14.6	13.1	9.3	6.9	**5**.7

4.3. Best Quantization Factor and Sampling Factor Setting in CQ

To find the best quantization factor S and sampling factor D, we compared the objective performance of image compression and the subjective quality of the decoded image under different S and D settings so that the CQ could obtain good compression performance while retaining the objects in the thin cloud-covered regions.

As can be seen from the objective performance of image compression in Table 3 and the subjective quality of decoded images in Figure 15, when the quantization factor S was fixed, the compression performance was better as the sampling factor D increased, and when the sampling factor D was fixed, the compression performance was better as the quantization factor S increased. In particular, when the sampling factor D reached the maximum value of 1024, it was equivalent to filling the cloudy regions with a single value, and the compression performance no longer changed as the quantization factor S increased.

The main purpose of this experiment was to find the best quantization factor S and sampling factor D values to achieve better compression performance while retaining the information of thin cloudy regions. Figure 15a is an RS image containing thin clouds. The red box on the left in the image is a road covered by thin clouds, and the red box on the right is a river covered by thin clouds. It can be seen that when D = 0 and S = 2, roads and rivers were still clearly visible. When S increased to four, since the gray value of the road was higher, it could still be distinguished, while the gray value of the river was lower and could no longer be accurately distinguished under a larger quantization factor. When S increased to six, neither roads nor rivers in the decoded image could be accurately distinguished. As a result, two was selected as the optimal value of the quantization factor S. When S

was two and D was increased to four, roads and rivers could still be distinguished in the decoded image. When D was increased to 16, serious blocking effects appeared, and roads and rivers could no longer be accurately distinguished in the decoded image, so 4 was selected as the best value of the sampling factor D.

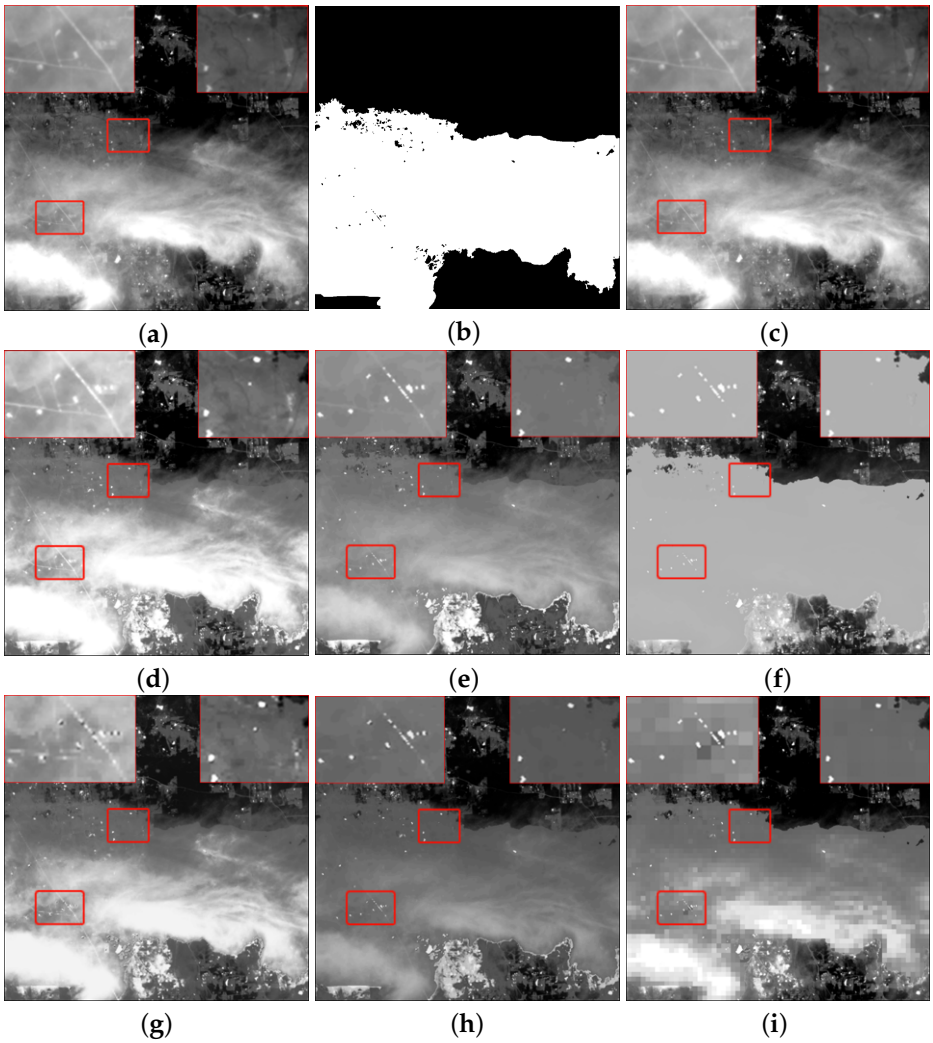


Figure 15. The decoded images by using CQ with different S and D values. The close-up views of the regions marked by red boxes are shown at the top right corner and the top left corner. (**a**) is original image, (**b**) is cloud mask of (**a**). (**c**) D = 0, S = 0, $PSNR_{ROI}$ = 60.14 dB, (**d**) D = 0, S = 2, $PSNR_{ROI}$ = 62.83 dB, (**e**) D = 0, S = 4, $PSNR_{ROI}$ = 63.54 dB, (**f**) D = 0, S = 6, $PSNR_{ROI}$ = 65.21 dB, (**g**) D = 4, S = 2, $PSNR_{ROI}$ = 63.01 dB, (**h**) D = 4, S = 4, $PSNR_{ROI}$ = 63.87 dB, (**i**) D = 16, S = 2, $PSNR_{ROI}$ = 63.95 dB.

Table 3. Coding performance evaluation of the CQ with different S and D values. The average percentage of clouds was 50%. The compression ratio was 4. Results report the $PSNR_{ROI}$ in dB.

$PSNR_{ROI}$ (dB)		**Quantization Factors S**					
		0	**2**	**4**	**6**	**8**	**10**
Sampling factors D	**0**	60.14	62.83	63.54	65.21	66.20	66.31
	4	61.75	63.01	63.87	65.54	66.24	66.41
	16	62.81	63.95	64.89	65.74	66.26	66.42
	64	63.51	64.85	65.79	65.98	66.38	66.46
	256	64.91	65.67	66.27	66.41	66.47	66.49
	1024	66.51	66.51	66.51	66.51	66.51	66.51

In summary, under the premise of considering the compression performance and the subjective quality of the decoded image at the same time, the optimal values of the quantization factor S and the sampling factor D were determined to be two and four, respectively. When S = 2 and D = 4, the $PSNR_{ROI}$ of the decoded image obtained by CQ was 63.01 dB, which was an increase of 4.8% compared with the performance without sampling and quantization (D = 0, S = 0), and the ground objects in the area covered by thin clouds were retained in the decoded image.

4.4. Comparisons of Image Compression Performance Before and After Optimizing DC-Level Shift

By analyzing the characteristics of cloud-covered remote sensing images, we improve the DC-level shift module in JPEG2000. The experiment in this section evaluated the compression performance of our method before and after improving the DC-level shift. The upward arrow signs and values in parentheses indicate the magnitude of the performance improvement after optimizing the DC-level shift.

It can be seen from Table 4 that after the OAF and CQ optimized the DC-level shift module in JPEG2000, the $PSNR_{ROI}$ was increased by a maximum of 3.46 dB and a minimum of 0.10 dB, and the compression performance was significantly improved. Therefore, it is meaningful to optimize the DC-level shift according to the characteristics of cloud-covered remote sensing images.

Table 4. Comparisons of image compression performance before and after the improved DC-level shift, the improved performance is indicated using ↑. The average percentage of cloud was 50%. Results report the $PSNR_{ROI}$ in dB.

$PSNR_{ROI}$ (dB)	**Compression Ratio**					
	2	**4**	**8**	**16**	**32**	**64**
CQ(D = 4, S = 2) + JPEG2000	127.61	62.51	54.92	47.94	42.55	37.67
CQ (D = 4, S = 2) + JPEG2000(DC_{opt})	127.82 (↑ 0.21)	64.76 (↑ 2.25)	55.02 (↑ 0.1)	48.13 (↑ 0.19)	42.66 (↑ 0.11)	37.83 (↑ 0.16)
OAF + JPEG2000	168.12	68.93	56.46	49.95	44.81	38.97
OAF + JPEG2000(DC_{opt})	168.54 (↑ 0.42)	72.39 (↑ 3.46)	56.65 (↑ 0.19)	50.08 (↑ 0.13)	45.13 (↑ 0.32)	39.12 (↑ 0.15)

4.5. Compression Performance Evaluation

We compared OAF (OAF + JPEG2000(DC_{opt})) and CQ (CQ + JPEG2000(DC_{opt})) with other existing methods, including JPEG2000, ADR (ADR + JPEG2000), and LEC (LEC + JPEG2000), using objective performance indicators $PSNR_{ROI}$ and the subjective visual quality of the decoded image, respectively. The wavelet transform in JPEG2000 employed a 9/7 wavelet. The number of test images was 360. The average percentage of cloudy regions included 30%, 50%, and 70%. The size of the image was 1024 × 1024. The image precision was 10 bits. Compression ratios included 2, 4, 8, 16, 32, and 64. The test results are shown in Tables 5–7. The best compression performance is indicated in bold. The down arrow signs and values in parentheses indicate the decreasing magnitude of the current performance compared to the best performance. The subjective quality comparisons of decoded images are shown in Figures 16–21. Image 1 contains thin clouds and thick clouds, and image 2 only contains thick clouds.

Tables 5–7 show the compression performance of our method and other methods for different percentages of clouds at different compression ratios. Figures 16–21 compares the compression performance of our method and other methods through the subjective visual quality of decoded images. Five important points are worth noting in these results.

(a) It was beneficial to apply image preprocessing for the coding of cloud-covered remote sensing images to enhance the coding efficiency. Under the same compression ratio, the higher the percentage of clouds, the better the compression performance.

Table 5. Comparisons of different image compression algorithms. The average percentage of clouds was 30%. Results report the $PSNR_{ROI}$ in dB. We bold the metrics corresponding to the best method and use ↓ and ↑ to indicate the improved and reduced performance between the best and the other methods.

$PSNR_{ROI}$ (dB)	**Compression Ratio**					
	2	**4**	**8**	**16**	**32**	**64**
JPEG2000	81.80 (↓ 36.93)	59.14 (↓ 3.11)	51.33 (↓ 1.94)	45.60 (↓ 1.65)	39.83 (↓ 2.28)	34.22 (↓ 2.42)
Ballé	85.62 (↓ 33.11)	67.18 (↑ 4.93)	61.74 (↑ 8.47)	54.38 (↑ 7.13)	48.77 (↑ 6.66)	44.67 (↑ 8.03)
BPG	89.12 (↓ 29.61)	76.46 (↑ 14.21)	72.05 (↑ 18.78)	69.47 (↑ 22.22)	64.22 (↑ 22.11)	58.66 (↑ 22.02)
ADR + JPEG2000	103.56 (↓ 15.17)	61.19 (↓ 1.06)	52.19 (↓ 1.08)	45.51 (↓ 1.74)	39.71 (↓ 2.40)	35.04 (↓ 1.60)
LEC + JPEG2000	108.00 (↓ 10.73)	61.83 (↓ 0.42)	52.89 (↓ 0.38)	46.50 (↓ 0.75)	40.82 (↓ 1.29)	36.10 (↓ 0.54)
CQ (D = 4, S = 2) + JPEG2000(DC_{opt})	92.53 (↓ 26.20)	60.82 (↓ 1.43)	52.21 (↓ 1.06)	45.71 (↓ 1.54)	40.46 (↓ 1.65)	35.51 (↓ 1.13)
CQ (D = 1024, S = 10) + JPEG2000(DC_{opt})	106.33 (↓ 12.40)	61.82 (↓ 0.43)	52.89 (↓ 0.38)	46.50 (↓ 0.75)	41.21 (↓ 0.90)	35.92 (↓ 0.72)
OAF + JPEG2000(DC_{opt})	**118.73**	**62.25**	**53.27**	**47.25**	**42.11**	**36.64**

Table 6. Comparisons of different image compression algorithms. The average percentage of cloud was 50%. Results report the $PSNR_{ROI}$ in dB. We bold the metrics corresponding to the best method and use ↓ and ↑ to indicate the improved and reduced performance between the best and the other methods.

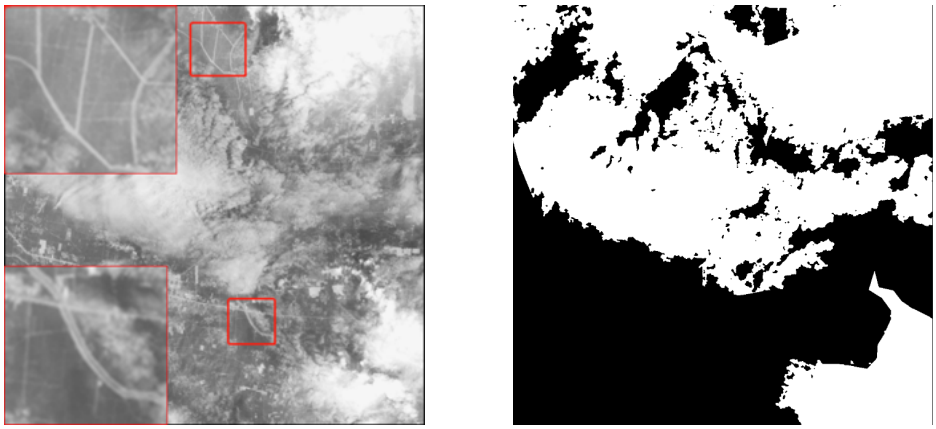
$PSNR_{ROI}$ (dB)	**Compression Ratio**					
	2	**4**	**8**	**16**	**32**	**64**
JPEG2000	90.04 (↓ 78.50)	60.14 (↓ 12.25)	52.26 (↓ 4.29)	46.74 (↓ 3.24)	39.80 (↓ 5.03)	33.17 (↓ 5.95)
Ballé	92.36 (↓ 76.18)	71.60 (↓ 0.79)	66.54 (↑ 9.99)	60.74 (↑ 10.76)	55.46 (↑ 10.63)	49.67 (↑ 10.55)
BPG	95.68 (↓ 72.86)	76.82 (↑ 4.43)	72.90 (↑ 16.35)	69.66 (↑ 19.68)	64.53 (↑ 19.7)	59.09 (↑ 19.97)
ADR + JPEG2000	166.77 (↓ 1.77)	67.31 (↓ 5.08)	55.46 (↓ 1.09)	48.25 (↓ 1.73)	40.60 (↓ 4.23)	34.98 (↓ 4.14)
LEC + JPEG2000	167.48 (↓ 1.06)	68.92 (↓ 3.47)	56.30 (↓ 0.25)	49.38 (↓ 0.60)	41.99 (↓ 2.84)	36.29 (↓ 2.83)
CQ (D = 4, S = 2) + JPEG2000(DC_{opt})	127.82 (↓ 40.72)	64.76 (↓ 7.63)	55.02 (↓ 1.53)	48.13 (↓ 1.85)	42.66 (↓ 2.17)	37.83 (↓ 1.29)
CQ (D = 1024, S = 10) + JPEG2000(DC_{opt})	167.16 (↓ 1.38)	68.60 (↓ 3.79)	56.29 (↓ 0.26)	49.38 (↓ 0.60)	43.89 (↓ 0.94)	38.64 (↓ 0.48)
OAF + JPEG2000(DC_{opt})	**168.54**	**72.39**	**56.55**	**49.98**	**44.83**	**39.12**

(b) For remote sensing images with different percentages of clouds, the proposed OAF achieved the best compression performance among all the compression algorithms. As shown in Tables 5–7, in the case of a four-time compression ratio, the performance of a 50% cloud-covered RS image compression using the OAF was increased by 20% and 5% compared to JPEG2000 and the current best-performing LEC method, respectively.

(c) The biggest advantage of the proposed CQ strategy was that it could retain the information of the ground objects under thin clouds while obtaining better compression performance. As shown in Table 5–7, compared with JPEG2000, the compression performance of the CQ was greatly improved. When the compression ratio was four, and the percentage of clouds was 50%, the $PSNR_{ROI}$ of the CQ (D = 4, S = 2) was increased by 7.7% compared to JPEG2000. With the increase in S and D, the compression performance continued to improve. When S and D reached the maximum value, the $PSNR_{ROI}$ of the CQ (D = 1024, S = 10) was increased by 14% compared to JPEG2000.

Table 7. Comparisons of different compression algorithms. The average percentage of clouds was 70%. Results report the $PSNR_{ROI}$ in dB. We bold the metrics corresponding to the best method and use ↓ and ↑ to indicate the improved and reduced performance between the best and the other methods.

$PSNR_{ROI}$ (dB)	**Compression Ratio**					
	2	**4**	**8**	**16**	**32**	**64**
JPEG2000	117.59 (↓ 51.91)	63.72 (↓ 60.70)	54.27 (↓ 9.18)	48.75 (↓ 4.92)	42.81 (↓ 5.03)	37.21 (↓ 4.78)
Ballé	117.88 (↓ 51.62)	73.90 (↓ 50.52)	69.23 (↑ 5.78)	64.02 (↑ 10.35)	57.78 (↑ 9.94)	51.25 (↑ 9.26)
BPG	119.42 (↓ 50.08)	80.31 (↓ 44.11)	75.18 (↑ 11.73)	71.46 (↑ 17.79)	65.39 (↑ 17.55)	62.27 (↑ 20.28)
ADR + JPEG2000	166.83 (↓ 2.67)	113.41 (↓ 11.01)	60.68 (↓ 2.77)	51.48 (↓ 2.19)	44.14 (↓ 3.70)	38.55 (↓ 3.44)
LEC + JPEG2000	166.99 (↓ 2.51)	118.09 (↓ 6.33)	62.12 (↓ 1.33)	52.85 (↓ 0.83)	45.94 (↓ 1.90)	40.40 (↓ 1.59)
CQ (D = 4, S = 2) + JPEG2000(DC_{opt})	161.12 (↓ 8.38)	74.89 (↓ 49.53)	59.43 (↓ 4.02)	51.13 (↓ 2.54)	45.00 (↓ 2.84)	40.00 (↓ 1.99)
CQ (D=1024, S=10) + JPEG2000(DC_{opt})	166.92 (↓ 2.58)	111.50 (↓ 12.92)	61.58 (↓ 1.87)	52.81 (↓ 0.86)	46.55 (↓ 1.29)	41.11 (↓ 0.88)
OAF + JPEG2000(DC_{opt})	**169.50**	**124.42**	**63.45**	**53.67**	**47.84**	**41.99**

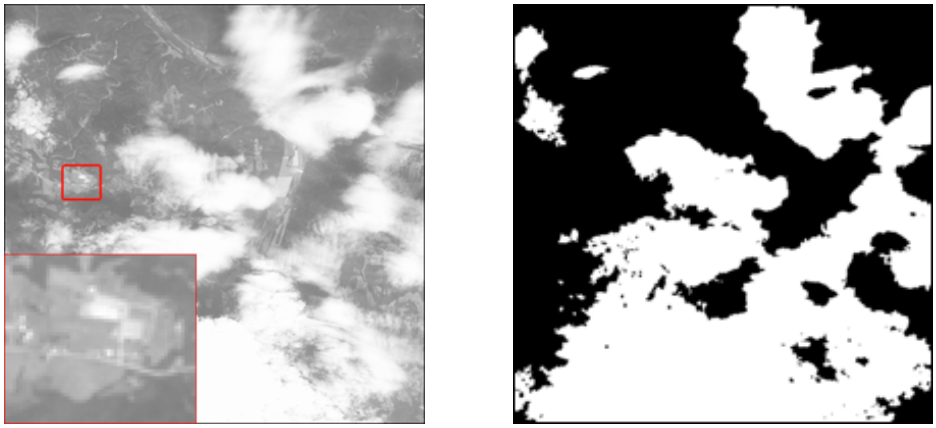


(**a**) (**b**)

Figure 16. Image 1.The percentage of clouds was 50%. (**a**) is original image, (**b**) is cloud mask of (**a**). The close-up views of the regions marked by red boxes are shown at the top left corner and the bottom left corner.

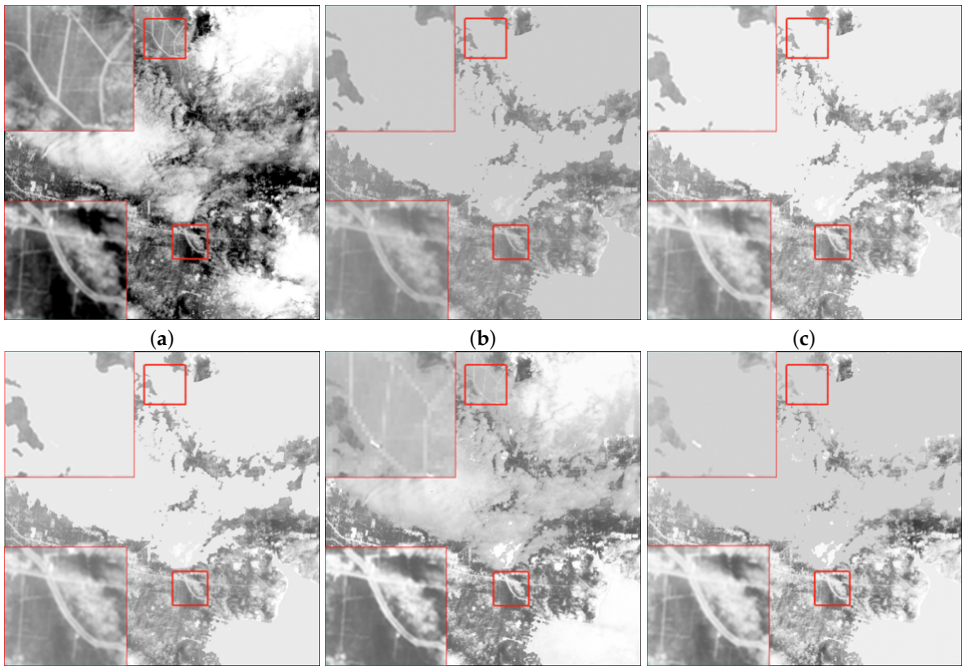
(d) For the CQ strategy, although it could not achieve the same compression performance as the OAF when S and D were set to the optimal value, the compression performance was still better than ADR and LEC at some compression ratios. For example, when the compression ratio was 32, and the percentage of clouds was 50%, the $PSNR_{ROI}$ of the CQ (D = 4, S = 2) was increased by 1.6% compared to LEC and by 5.1% compared to ADR. When the compression ratio was 64 and the percentage of clouds was 50%, the $PSNR_{ROI}$ of the CQ (D = 4, S = 2) was increased by 4.2% compared to LEC and by 8.1% compared to ADR.

(e) The CQ could retain the information of the ground objects under thin clouds when S and D were set to the optimal value. The compression performance of the CQ was almost equal to the OAF when D = 1024 and S = 10, but the ground objects under thin clouds were lost. We could achieve different compression performance values by flexibly adjusting the values of S and D, so CQ was more flexible than OAF.



(**a**) (**b**)

Figure 17. Image 2. The percentage of could was 50%. (**a**) is original image, (**b**) is cloud mask of (**a**). The close-up views of the regions marked by red boxes are shown at the bottom left corner.



(**a**) (**b**) (**c**)

(**d**) (**e**) (**f**)

Figure 18. Comparison of subjective quality of decoded image 1. The close-up views of the regions marked by red boxes are shown at the bottom left corner and the top left corner. The compression ratio was 4. (**a**) JPEG2000 $PSNR_{ROI}$ = 61.98 dB, (**b**) ADR + JPEG2000 $PSNR_{ROI}$ = 65.61 dB, (**c**) LEC + JPEG2000 $PSNR_{ROI}$ = 66.48 dB, (**d**) OAF + JPEG2000(DC_{opt}) $PSNR_{ROI}$ = 67.75 dB, (**e**) CQ (D = 4, S = 2) + JPEG2000(DC_{opt}) $PSNR_{ROI}$ = 64.70 dB, (**f**) CQ (D = 1024, S = 10) + JPEG2000(DC_{opt}) $PSNR_{ROI}$ = 67.18 dB.

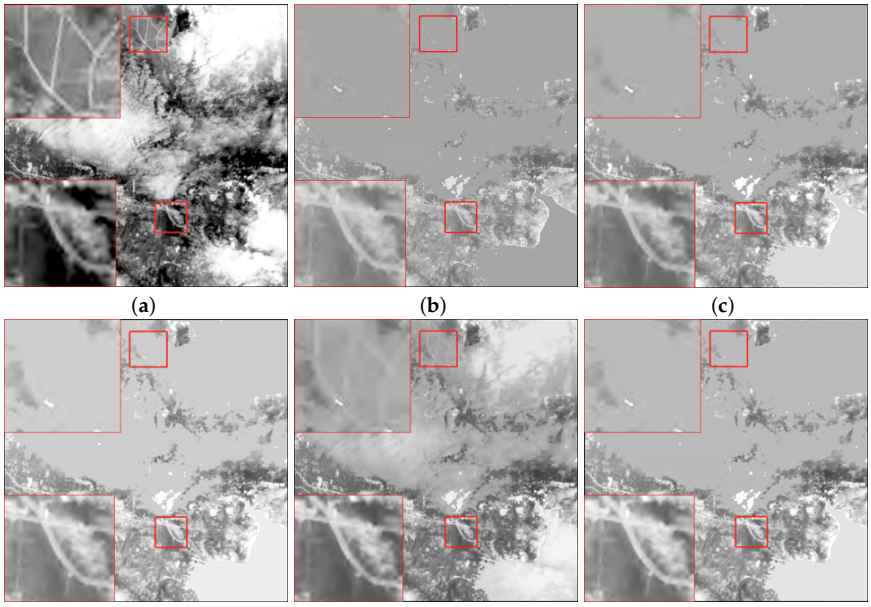


Figure 19. Comparison of subjective quality of the decoded image of image 1. The close-up views of the regions marked by red boxes are shown at the bottom left corner and the top left corner. The compression ratio was 64. (**a**) JPEG2000. $PSNR_{ROI}$ = 32.76 dB, (**b**) ADR + JPEG2000 $PSNR_{ROI}$ = 32.98 dB, (**c**) LEC + JPEG2000 $PSNR_{ROI}$ = 33.50 dB, (**d**) OAF + JPEG2000(DC_{opt} $PSNR_{ROI}$ = 34.97 dB, (**e**) CQ (D = 4, S = 2) + JPEG2000(DC_{opt}) $PSNR_{ROI}$ = 33.45 dB, (**f**) CQ (D = 1024, S = 10) + JPEG2000(DC_{opt}) $PSNR_{ROI}$ = 34.04 dB.

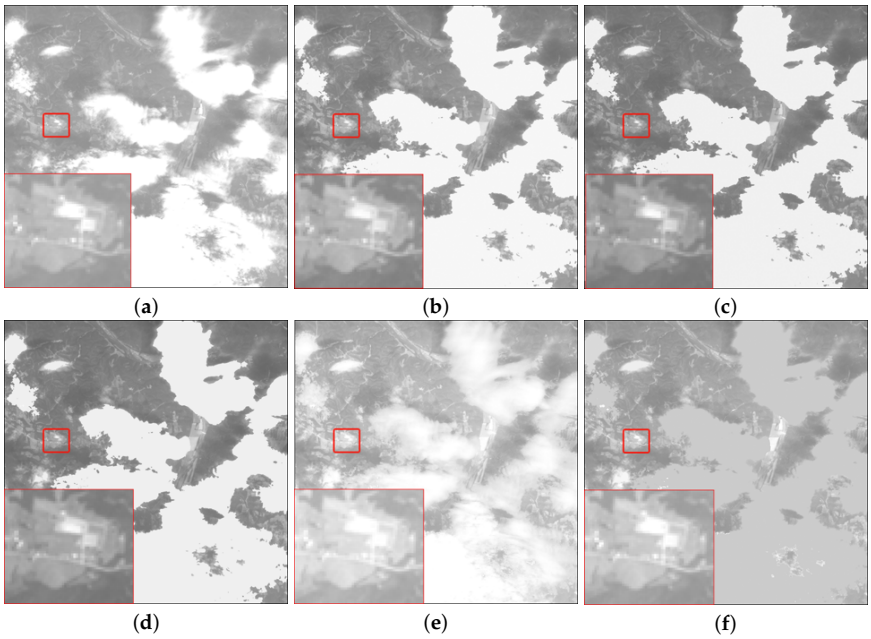


Figure 20. Comparison of subjective quality of the decoded image of image 2. The close-up views of the regions marked by red boxes are shown at the bottom left corner and the top left corner. The compression ratio was 4. (**a**) JPEG2000. $PSNR_{ROI}$ = 61.84 dB, (**b**) ADR + JPEG2000 $PSNR_{ROI}$ = 64.55 dB, (**c**) LEC + JPEG2000 $PSNR_{ROI}$ = 66.71 dB, (**d**) OAF + JPEG2000(DC_{opt}) $PSNR_{ROI}$ = 69.69 dB, (**e**) CQ (D = 4, S = 2) + JPEG2000(DC_{opt}) $PSNR_{ROI}$ = 65.22 dB, (**f**) CQ (D = 1024, S = 10) + JPEG2000(DC_{opt}) $PSNR_{ROI}$ = 69.01 dB.

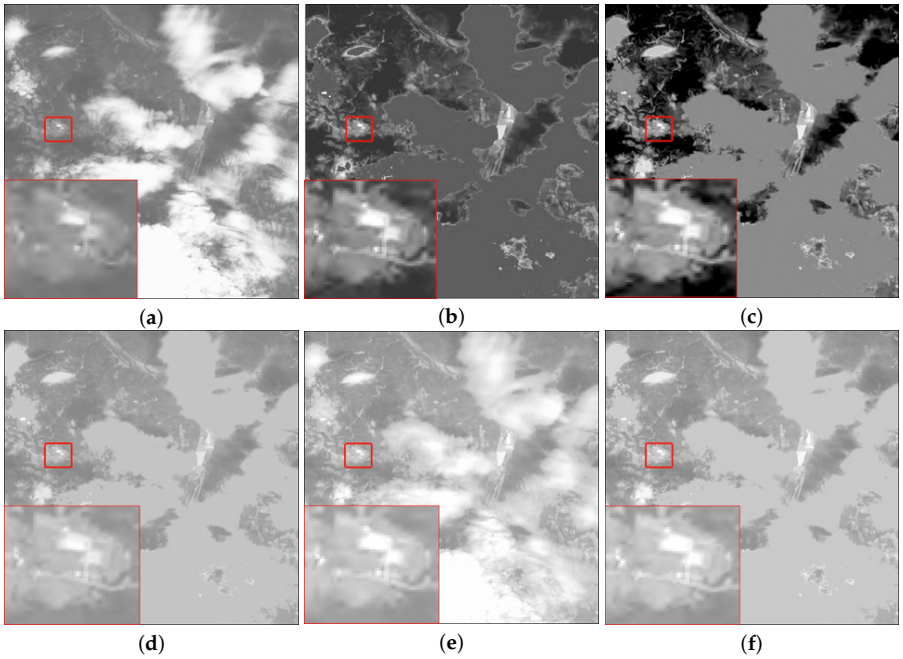


Figure 21. Comparison of subjective quality of the decoded image of image 2. The close-up views of the regions marked by red boxes are shown at the bottom left corner. The compression ratio was 64. (**a**) JPEG2000. $PSNR_{ROI}$ = 28.45dB, (**b**) ADR + JPEG2000 $PSNR_{ROI}$ = 32.38 dB, (**c**) LEC + JPEG2000 $PSNR_{ROI}$ = 33.73 dB, (**d**) OAF + JPEG2000(DC_{opt}) $PSNR_{ROI}$ = 36.53 dB, (**e**) CQ (D = 4, S = 2) + JPEG2000(DC_{opt}) $PSNR_{ROI}$ = 33.82 dB, (**f**) CQ (D = 1024, S = 10) + JPEG2000(DC_{opt}) $PSNR_{ROI}$ = 36.13 dB.

5. Discussion

5.1. Suitability for On-Board Compression

At present, there are still many difficulties in satellite image compression at the application level. First, the quantity of on-board image data is usually large, and the compression algorithm is required to have a high compression ratio when the satellite transmission bandwidth is limited. Secondly, due to the limited computing resources of the satellite, the compression algorithm needs to have a lower computational complexity to improve the speed of on-board compression. Finally, the on-board image compression algorithm should be easy to implement and compatible with different device platforms [37,38].

Combined with the above analysis of satellite image compression requirements, the more typical algorithms used for on-board image compression include CCSDS and JPEG2000, of which JPEG2000 is the most widely used on-board image compression algorithm. Although the complexity of CCSDS is slightly lower than that of JPEG2000, its compression performance is more different than that of JPEG2000 [19,39]. Therefore, JPEG2000 is widely used in satellite image compression, such as China's launch of the Tianwen-1 satellite, Remote Sensing 8 satellite, Turkey's launch of the BilSAT-1 satellite, and the Rasat satellite; they all use the JPEG2000 compression algorithm.

In the actual satellite image compression scenario, a cloud region is inevitable in optical remote sensing images, and existing image compression methods often directly compress cloud-containing regions, which consumes a considerable amount of coding bit rate and lead to poor reconstruction quality of the region of interest, so the compression performance can be effectively improved by removing or reducing the data of cloud-covered regions through reasonable preprocessing methods.

In this paper, we combined the JPEG2000 algorithm with the proposed OAF and CQ preprocessing strategies to further reduce the coding cost without introducing higher complexity, which is more suitable for spaceborne image compression applications.

5.2. Universality Evaluation

To illustrate the universality of the OAF and CQ strategies, we combined OAF and CQ with other compression frameworks. We chose a traditional compression method, BPG [40], and a deep learning-based method from Ballé [41], because both of them are currently widely used and representative image compression methods.

The experimental results are shown in Tables 8–10. It can be seen that for both BPG [40] and Ballé's method [41], the higher the percentage of cloud in the remote sensing image, the better the compression performance at the same compression ratio. The proposed OAF strategy was the most effective among all the methods. The lower the compression ratio for cloudy images, the more effective our preprocessing strategy was on the compression performance. Even if the compression ratio was increased to 64, the compression performance could still be improved by using our preprocessing strategy.

The experimental results demonstrated that the OAF and CQ strategies were highly compatible with different image compression frameworks. Under images with different percentages of clouds and different compression ratios, the OAF and CQ strategies could both improve compression performance.

Table 8. Experimental results of BPG and Ballé's method. The average percentage of cloud was 30%.We bolded the metrics with the highest PSNR.

$PSNR_{ROI}$ (dB)	Compression Ratio					
	2	**4**	**8**	**16**	**32**	**64**
Ballé	85.62	67.18	61.74	54.38	48.77	44.67
CQ(D = 4, S = 2) + Ballé	93.90	68.43	63.59	55.27	49.64	44.89
OAF + Ballé	119.63	72.23	66.82	58.29	51.38	45.06
BPG	89.12	76.46	72.05	69.47	64.22	58.66
CQ(D = 4, S = 2) + BPG	97.89	77.85	73.29	69.58	64.91	58.89
OAF + BPG	121.55	80.72	76.02	71.37	65.80	60.59

Table 9. Experimental results of BPG and Ballé's method. The average percentage of cloud was 50%.We bolded the metrics with the highest PSNR.

$PSNR_{ROI}$ (dB)	Compression Ratio					
	2	**4**	**8**	**16**	**32**	**64**
Ballé	92.36	71.60	66.54	60.74	55.46	49.67
CQ (D = 4, S = 2) + Ballé	114.39	73.21	69.92	61.98	57.56	51.02
OAF + Ballé	160.58	76.60	71.85	63.06	58.62	51.99
BPG	95.68	76.82	72.90	69.66	64.53	59.09
CQ (D = 4, S = 2) + BPG	124.54	80.03	75.62	71.17	67.28	60.72
OAF + BPG	165.17	89.14	77.34	73.67	68.98	62.28

To further test the generality of our proposed method, we looked for some other datasets on cloud region detection, such as Sentinel-2A, WHUS2-CD, CloudSEN12 [17]; we downloaded the Sentinel-2 cloud mask dataset and randomly selected 120 sub-scene images from it, with the resolution of 512 × 512. The image precision was 8 bits. Compression ratios included 2, 4, 8, 16, 32, and 64. The test results are shown in Table 11.

According to the results in the Table 11, our proposed preprocessing strategies effectively improved the compression performance under different datasets, among which our proposed OAF strategy had the best compression performance, and OAF improved the PSNR performance by nearly 30% compared to JPEG2000 at an eight-time compression ratio. The CQ strategy did not improve the compression performance as significantly as the OAF strategy, but it had a certain degree of improvement at all compression ratios

compared to JPEG2000. These results demonstrate that our proposed method is equally versatile on different datasets.

Table 10. Experimental results of BPG and Ballé's method. The average percentage of cloud was 70%.We bolded the metrics with the highest PSNR.

$PSNR_{ROI}$ (dB)	Compression Ratio					
	2	**4**	**8**	**16**	**32**	**64**
Ballé	117.88	73.90	69.23	64.02	57.78	51.25
CQ (D = 4, S = 2) + Ballé	149.84	81.19	74.40	68.67	60.32	54.27
OAF + Ballé	163.15	110.77	79.29	72.08	62.96	56.34
BPG	119.42	80.31	75.18	71.46	65.39	62.27
CQ (D = 4, S = 2) + BPG	156.32	92.41	80.92	76.47	69.25	64.29
OAF + BPG	167.55	115.69	84.77	79.42	74.25	69.14

Table 11. Experimental results on the Sentinel-2 cloud mask dataset.We bolded the metrics with the highest PSNR.

$PSNR_{ROI}$ (dB)	Compression Ratio					
	2	**4**	**8**	**16**	**32**	**64**
JPEG2000	86.03	71.07	49.41	43.28	38.91	36.16
CQ (D = 4, S = 2) + JPEG2000	87.90	72.76	52.36	44.18	38.93	36.19
OAF + JPEG2000	88.68	83.30	64.16	53.00	44.27	40.32

5.3. Analysis of Selection Mechanisms for OAF and CQ Modules

Regarding the selection of OAF and CQ modules, our current approach is to manually select the OAF module or the CQ module according to the category of clouds in remote sensing images and the requirements of application.

Specifically, the OAF strategy can completely remove the information of the cloudy region and minimize their coding consumption by leveraging the local edge characteristics of cloudy region in remote sensing images. For images only containing thick clouds, or for applications seeking minimal coding bit rates, it is suitable to choose the OAF module.

Contrarily, the CQ strategy implicitly identifies thin and thick clouds and rationally quantifies the data in cloudy regions by leveraging the characteristics of the distribution of thick and thin clouds and information redundancy in cloudy regions. The CQ strategy not only eliminates invalid information and reduces coding consumption but also retains partial information of ground objects in thin cloud-covered regions, which can balance compression efficiency and reconstructed image quality. Therefore, for images containing complex and diverse clouds, e.g., images mainly containing thin clouds or both containing thin and thick clouds, or for applications that require retaining valuable information of the cloudy regions, it is more appropriate to choose the CQ module.

The limitation of our manual selection mechanism is that it is not adaptive and cannot satisfy all application scenarios. How to adaptively select the OAF module or the CQ module is left for future research.

6. Conclusions

This paper proposed two preprocessing strategies for invalid cloud-covered remote sensing image compression, namely, the OAF strategy and the CQ strategy. Both strategies can be embedded into any existing compression methods to control the coding rate allocation of the data in cloudy and cloud-free regions, which can improve the quality of decoded images. The OAF strategy uses the mean of the inner and outer edge contexts to fill cloudy regions and then performs mean filtering on the boundary of the filled cloudy regions. Experimental results showed that OAF achieved better performance than the preprocessing strategies of existing image compression methods. The CQ strategy can implicitly identify

thin clouds and thick clouds by setting a quantization factor (S) and a sampling factor (D) to quantize the data of cloudy regions in both the amplitude domain and the spatial domain. CQ achieves different compression performance values by adjusting S and D, which can meet the needs of different tasks. Moreover, an efficient binary cloud mask coding algorithm was developed to enhance the contrast of decoded images, which effectively improved the subjective visual quality of decoded images.

7. Patents

Wang K Y, Wang X S, Li Y S, et al. A Cloud-Covered Remote Sensing Image Compression Method Based on Filling Strategy: CN112465846B.X[P]. 7 April 2023.

Wang K Y, Gu D W, Li Y S, et al. A Cloud-Covered Remote Sensing Image Compression Method Based on Quantization Strategy: CN112565756B.X[P]. 26 March 2023.

Author Contributions: Methodology, K.W., J.J. and L.Y.; software, L.Y., J.J. and H.M.; validation, K.W. and K.L.; investigation, K.W., J.J. and K.L.; writing—original draft preparation, K.W., J.J. and P.Z.; writing—review and editing, K.W. and P.Z.; supervision, K.W. and P.Z.; project administration, K.W. and Y.L.; funding acquisition, K.W., P.Z. and Y.L. All authors have read and agreed to the published version of the manuscript.

Funding: This research was funded in part by the National Natural Science Foundation of China grant number 62121001, in part by the Science and Technology on Electromechanical Dynamic Control Laboratory, China grant number 6142601220302, in part by the Natural Science Basic Research Program of Shaanxi grant number 2024JC-YBQN-0635, and in part by the Fundamental Research Funds for the Central Universities grant number XJSJ23087.

Data Availability Statement: The original contributions presented in the study are included in the article; further inquiries can be directed to the corresponding author.

Acknowledgments: We thank the reviewers for their valuable feedback on this paper.

Conflicts of Interest: The authors declare no conflicts of interest.

References

1. Yuan, W.; Lining, X. Remote sensing satellite networking technology and remote sensing system: A survey. *IEEE Int. Conf. Electron. Meas. Instruments (ICEMI)* **2015**, *3*, 1251–1256.
2. Joshi, V.; Rani, J.S. A simple lossless algorithm for on-board satellite hyperspectral data compression. *IEEE Geosci. Remote Sens. Lett.* **2023**, 20, 5504305 . [CrossRef]
3. Kucherov, B.; Přibyl, O.; Artyushenko, V. Increasing efficiency of getting results of satellite remote sensing for smart cities. In Proceedings of the Smart City Symposium Prague (SCSP), Prague, Czech Republic, 25–26 May 2017; pp. 1–6.
4. Zhang, Y.; Rossow, W.B.; Lacis, A.A.; Oinas, V.; Mishchenko, M.I. Calculation of radiative fluxes from the surface to top of atmosphere based on ISCCP and other global data sets: Refinements of the radiative transfer model and the input data. *J. Geophys. Res. Atmos.* **2004**, *109*, D19105. [CrossRef]
5. Huang, B. *Satellite Data Compression*; Springer Science and Business Media: Berlin/Heidelberg, Germany, 2011.
6. Rabbani, M.; Joshi, R.L.; Jones, P.W. JPEG 2000 core coding system (Part 1). *Jpeg 2000 Suite* **2009**, *15*, 1.
7. *ISO/IEC, 2002: 15444-10*; Information Technology Jpeg 2000 Image Coding System: Extensions for Three-Dimensional Data. ISO: Geneva, Switzerland. 2002.
8. Li, S.; Li, W. Shape-adaptive discrete wavelet transforms for arbitrarily shaped visual object coding. *IEEE Trans. Circuits Syst. Video Technol.* **2000**, *10*, 725–743.
9. Gonzalez-Conejero, J.; Serra-Sagrista, J.; Rubies-Feijoo, C.; Donoso-Bach, L. Encoding of images containing no-data regions within JPEG2000 framework. In Proceedings of the IEEE International Conference on Image Processing, San Diego, CA, USA, 12–15 October 2008; pp. 1057–1060.
10. Wang, H.; Zhou, H.; Wang, J. An invalid cloud region masking method for remote sensing image compression. *Pattern Recognit. Image Anal.* **2020**, *30*, 134–144. [CrossRef]
11. Oktem, R.; Benderli, O.; Ismailoğlu, N. Improving compression ratio for satellite transmission by use of cloud extraction. In Proceedings of the European Signal Processing Conference, Antalya, Turkey, 2005; pp. 1–4.
12. Campbell, J.B.; Wynne, R.H. *Introduction to Remote Sensing*; Guilford Press: New York, NY, USA, 2011.
13. Zhao, Y. *Principles and Methods of Remote Sensing Application Analysis*; Science Press: Beijing, China, 2003.
14. Gao, B.C.; Li, R.R. Removal of thin cirrus scattering effects in Landsat 8 OLI images using the cirrus detecting channel. *Remote Sens.* **2017**, *9*, 834. [CrossRef]

15. Barrett, E.C.; Grant, C.K. The Identification of Cloud Types in LANDSAT MSS Images. [Great Britain]. No. E76-10277. 1976. Available online: https://api.semanticscholar.org/CorpusID:126749179 (accessed on 10 July 2024).
16. Zhu, Z.; Woodcock, C.E. Object-based cloud and cloud shadow detection in Landsat imagery. *Remote Sens. Environ.* **2012**, *118*, 83–94. [CrossRef]
17. Zhang, J.; Shi, X.; Wu, J.; Song, L.; Li, Y. Cloud Detection Method based on Spatial-Spectral Features and Encoder-Decoder Feature Fusion. *IEEE Trans. Geosci. Remote Sens.* **2023**, *61*, 5407915. [CrossRef]
18. Zhang, J.; Song, L.; Wang, Y.; Wu, J.; Li, Y. Attention Mechanism With Spatial Spectrum Dense Connection and Context Dynamic Convolution for Cloud Detection. *IEEE Trans. Geosci. Remote Sens.* **2023**, *61*, 5408211. [CrossRef]
19. Shihab, H.S. Image compression techniques on-Board small satellites. *Iraqi J. Sci.* **2023**, 1518–1534. [CrossRef]
20. Gupta, D.; Choubey, S. Discrete wavelet transform for image processing. *Int. J. Emerg. Technol. Adv. Eng.* **2015**, *4*, 598–602.
21. Fisher, Y. Fractal image compression. *Fractals* **1994**, *2*, 347–361. [CrossRef]
22. Tekalp, A.M. *Digital Video Processing*; Prentice Hall Press: Hoboken, NJ, USA, 2015.
23. Tan, K.; Zhang, Y.; Tong, X.; Kang, Y. Automatic cloud detection for Chinese high resolution remote sensing satellite imagery. *Acta Geod. Cartogr. Sin.* **2016**, *45*, 581.
24. Suzuki, K.; Horiba, I.; Sugie, N. Linear-time connected-component labeling based on sequential local operations. *Comput. Vis. Image Underst.* **2003**, *89*, 1–23. [CrossRef]
25. He, L.; Zhao, X.; Yao, B.; Yang, Y.; Chao, Y.; Shi, Z.; Suzuki, K. A combinational algorithm for connected-component labeling and Euler number computing. *J.-Real-Time Image Process.* **2017**, *13*, 703–712. [CrossRef]
26. He, L.; Zhao, X.; Chao, Y.; Suzuki, K. Configuration-transition-based connected-component labeling. *IEEE Trans. Image Process.* **2013**, *23*, 943–951.
27. Ding, J.J.; Lee, P.X. Fast morphology algorithm with parallel processing structures. In Proceedings of the International Conference on Audio, Language and Image Processing, Shanghai, China, 7–9 July 2014; pp. 324–329.
28. Wu, Z.J.; Wu, L.H.; Yuan, B.F. Algorithm for detection of ROI based on fractal and wavelet. *J. Comput. Appl.* **2010**, *30*, 1613. [CrossRef]
29. Li, Z.; Yin, L.; Zhang, L. An improved rectangular partition coding for binary image. *Comput. Appl. Softw.* **2011**, *28*, 256–259.
30. Wang, P.; Yang, Y.; Yang, J. Image compression based on block encoding. *Comput. Eng. Des.* **2004**, 975–977. [CrossRef]
31. Shen, L.; Zhuo, L. *Wavelet Coding and Network Video Transmission*; Science Press: Beijing, China, 2005.
32. Xu, Z. *Research on Image Compression for Reginon of Interest of Remote Sensing Image Based on CCSDS*; Changchun Institute of Optics, Fine Mechanics and Pyhsics, Chinese Academy of Sciences: Changchun, China, 2014.
33. Giorgio, M.; Guida, M.; Pulcini, G. The transformed gamma process for degradation phenomena in presence of unexplained forms of unit-to-unit variability. *Qual. Reliab. Eng. Int.* **2018**, *34*, 543–562. [CrossRef]
34. Li, Z.; Shen, H.; Li, H.; Xia, G.; Gamba, P.; Zhang, L. Multi-feature combined cloud and cloud shadow detection in GaoFen-1 wide field of view imagery. *Remote Sens. Environ.* **2017**, *191*, 342–358. [CrossRef]
35. Smith, Craig M. Efficient Software Implementation of the JBIG Compression Standard. Online Version of Thesis, 1993. Available online: https://repository.rit.edu/theses/174/ (accessed on 10 July 2024).
36. Khan, A. Algorithm Study and Matlab Model for CCITT Group4 TIFF Image Compression. 2011. Available online: https://urn.kb.se/resolve?urn=urn:nbn:se:liu:diva-65709 (accessed on 10 July 2024).
37. Gunasheela, K.S.; Prasantha, H.S. Satellite image compression-detailed survey of the algorithms. In *Proceedings of International Conference on Cognition and Recognition: ICCR 2016*; Springer: Singapore, 2018; pp. 187–198.
38. Hassan, F.E.; Salama, G.I.; Ibrahim, M.S.; Bahy, R.M. Investigation of On-Board Compression techniques for Remote Sensing Satellite Imagery. In Proceedings of the International Conference on Aerospace Sciences and Aviation Technology, Capua, Italy, 17–19 May 2005; The Military Technical College: El Weili, Egypt, 2011; Volume 11, pp. 937–946.
39. Indradjad, A.; Nasution, A.S.; Gunawan, H.; Widipaminto, A. A comparison of Satellite Image Compression methods in the Wavelet Domain. In *IOP Conference Series: Earth and Environmental Science*; IOP Publishing: Bristol, UK, 2019; Volume 280, p. 012031.
40. Bellard, F. BPG Image Format. Available online: http://bellard.org/bpg/ (accessed on 30 January 2017).
41. Ballé, J.; Minnen, D.; Singh, S.; Hwang, S.J.; Johnston, N. Variational image compression with a scale hyperprior. In Proceedings of the International Conference on Learning Representations, Vancouver, BC, Canada, 30 April–3 May 2018.

Disclaimer/Publisher's Note: The statements, opinions and data contained in all publications are solely those of the individual author(s) and contributor(s) and not of MDPI and/or the editor(s). MDPI and/or the editor(s) disclaim responsibility for any injury to people or property resulting from any ideas, methods, instructions or products referred to in the content.